Time-dependent surface topography in a coupled crust–mantle convection model

Russell N. Pysklywec and M. Hosein Shahnas

Department of Geology, University of Toronto, 22 Russell Street, Toronto, Ontario M5S 3B1, *Canada. E-mail: russ@geology.utoronto.ca*

SUMMARY

Recent geodynamic research has shown that convective flow in the mantle may have an important role in the development of long-wavelength surface topography. This flow-induced 'dynamic topography' is usually derived from mantle convection models by computing the vertical component of hydrodynamic stress at the top of the model and assuming the stress is compensated by deflection of the surface. However, these models have generally ignored the presence of an overlying buoyant crust and its deformational response to the mantle flow. We consider the effects of horizontal convective forcing on the crust and investigate how this crust/lithosphere deformation interacts with the vertical component of mantle flow-induced subsidence/uplift at the surface. In particular, we test the response of various rheologies of the crust and mantle lithosphere to an episode of mantle downwelling. The evolution of crustal thickness and topography is tracked using thermomechanical numerical models of the crust–mantle system with a free surface upper boundary. A strong crust ($\eta_c = 2.5 \times 10^{25}$ Pa s) does not experience significant internal deformation and subsides above a mantle downwelling. For a weaker crust ($\eta_c < =10^{23}$ Pa s), descending mantle flow initially induces subsidence, but there is an inversion to surface uplift as crustal thickening induced by convergent mantle flow overcomes the dynamic subsidence. The presence of a strong mantle lithosphere, however, may effectively shield a weak crust from deformation imposed by the underlying horizontal mantle convective stresses. With temperature-dependent rheologies in the model, the interplay of the vertical/horizontal mantle forcings with the thermal evolution of the crust results in a highly time-dependent signal of topography. Subsequent to crustal thickening and uplift, the system may undergo rapid topographic subsidence and crustal thinning by localized channel flow in the hot and weak lower crust. These results suggest an alternative interpretation for the development of mantle-flow induced topography in certain tectonic environments.

Key words: geodynamics, lithospheric deformation, mantle convection, numerical techniques, plate tectonics, topography.

1 INTRODUCTION

Geodynamic modelling has provided important insight into the influence of mantle convective flow on the evolution of the overlying lithosphere. Early mantle convection models determined that normal stresses associated with the fluid motion can cause appreciable surface topography (McKenzie *et al.* 1974; McKenzie 1977). Global predictions of this 'dynamic topography' have been derived based on instantaneous flow calculations from interpretations of seismic tomography (e.g. Hager *et al.* 1985; Forte *et al.* 1993; Thoraval *et al.* 1995). Such studies suggest, for example, that dynamic topography may play a role in the formation of large-scale sedimentary basins. In particular, mantle flow induced by subducting slabs can cause significant subsidence at a plate margin (e.g. Mitrovica *et al.* 1989; Gurnis 1992; Stern & Holt 1994; Russell & Gurnis 1994;

Pysklywec & Mitrovica 1999) and within continental interiors (Pysklywec & Mitrovica 1998; Pysklywec & Quintas 2000). Connections between mantle convection and dynamic uplift have also been established to reconcile the large-scale topographic high in southern Africa (Hager 1984; Lithgow-Bertelloni & Silver 1998; Gurnis *et al.* 2000). In general, these mantle flow models neglect the presence of an overlying buoyant crust and derive dynamic topography in an *a posteriori* calculation as the instantaneous vertical deflection of a surface that would be supported by the normal stresses computed at the top (fixed) boundary of the convection space (e.g. McKenzie *et al.* 1974).

However, mantle convection also induces significant tangential stresses at the base of the lithosphere. The rise of hot buoyant material and subduction of dense cold slabs (i.e. the thermal boundary layers of the mantle circulation), for example, drive horizontal

motions of the lithospheric plates (Hager & O'Connell 1981). At the surface, the Earth's buoyant crust responds to both horizontal and vertical forcings associated with mantle convection. Therefore, the corresponding surface topography would be governed by the total mantle flow, rather than the vertical component of fluid convection alone. Subsidence/uplift of the crust's surface induced by vertical convective stresses develops essentially instantaneously relative to the timescales associated with most tectonic regimes (Zhong *et al.* 1996). Horizontal convective stresses may cause cumulative deformation of the crust over geological timescales, most significantly at plate boundaries, but also in the plate interior. The interplay between these forcings may produce a unique crustal evolution and associated signal of surface topography.

Crustal deformation and the evolution of surface topography have been considered during episodes of gravitational instability of the lithosphere (Fleitout & Froidevaux 1982; Marotta *et al.* 1999; Neil & Houseman 1999). Neil & Houseman (1999), for example, formulated two-layer models of the lithosphere and considered how a Rayleigh–Taylor instability of the dense mantle lithosphere layer evolves and drives deformation of an overlying buoyant crustal layer. Their results show that shear stresses associated with the lithospheric instability can cause thickening of the crust which they suggest as a potential mechanism for intraplate orogeny. The models do not consider sublithospheric dynamics and, thus, do not take into account potentially important forcings from a convecting mantle.

Recently, mantle convection models of large-scale plate tectonics have been designed to study the horizontal motion of the lithosphere and the evolution of rigid surface plates (Bercovici 1998; Moresi & Solomatov 1998; Tackley 1998; Trompert & Hansen 1998; Tackley 2000a,b; Bercovici *et al.* 2001). These studies implement various material rheologies to simulate a 'plate-like' behaviour of the lithosphere, however, these models do not include a buoyant deformable crust or consider the resultant flow-induced surface topography.

Numerical modelling applied to tectonics on Venus provided some of the first insights into the coupled interaction between mantle convection and crustal dynamics (Lenardic *et al.* 1993, 1995; Smrekar & Parmentier 1996). Lenardic *et al.* (1995), for example, showed that mantle downwelling may drive crustal thickening (and inferred plateau formation) depending on the rheology of the basaltic crust. Coupled crust–mantle modelling also demonstrates that the deforming crust may in turn alter the style of the underlying mantle flow, as dynamically thickened crust can introduce significant changes in the thermal/mechanical state at the crust–mantle interface (Lenardic & Kaula 1995, 1996).

Several crust–mantle modelling studies have considered the topographic surface expression associated with mantle convection. 3-D simulations of time-dependent mantle convection that include a buoyant overlying crust demonstrate variable crustal accumulation and thickening above downwelling mantle flow (Moresi & Lenardic 1997, 1999). The resulting high positive topography in these regions is not in (Airy) isostatic equilibrium, as the crustal thickening is dynamically supported by the time-varying flow-induced convergence. These results indicate a more complex response of crustal topography to mantle convective flow than models which neglect the dynamic response of the buoyant crust. The models, however, are isoviscous and it would be expected that with a stronger crust and/or mantle lithosphere the crust may respond very differently to convective mantle flow (Moresi & Lenardic 1997). Zhong (1997) considered relaxation of crustal topography in a crust–mantle model using more complex visco-elastic rheologies. The results similarly

show that time-varying overcompensated topography can develop under the influence of sublithospheric loading, but the analyses impose a constant mantle buoyancy load and consequently neglect the influence of time-dependent convection in the underlying mantle.

The purpose of this work is to use numerical models of the coupled crust–mantle system to investigate the evolution of the crust and surface topography under the influence of a simple time-dependent driving mantle flow. The model crust is free to respond to the horizontal and vertical stresses associated with the underlying mantle flow (and, in turn, influence the convective flow). We build on the previous studies of crust–mantle convection by testing various rheologies for the crust and mantle lithosphere such as stratified isoviscous layers and temperature-dependent viscosities. The development of surface topography and variations crustal thickness are tracked during the experiments to gain insight into the time-dependent deformation of the crust.

2 SET-UP OF THE NUMERICAL MODEL

A set of numerical experiments was designed to study the time-dependent interaction of the coupled lithosphere-mantle system. Neglecting inertial terms (owing to extremely high Prandtl number of the mantle) and compressibility, the governing thermomechanical equations for our plane-strain model are:

$$\nabla \cdot \boldsymbol{\sigma} + \rho \mathbf{g} = 0 \tag{1}$$

$$\rho c_p \frac{DT}{Dt} - k\nabla \cdot \nabla T = 0 \tag{2}$$

$$\nabla \cdot \mathbf{v} = 0. \tag{3}$$

The equations are solved for temperature T and the velocity field $\mathbf{v}$. The stress tensor is given by $\boldsymbol{\sigma}$, c_p is the specific heat at constant pressure, k is the thermal conductivity, and $\mathbf{g}$ is the vector gravitational acceleration. The density, ρ is given by the equation of state,

$$\rho(T) = \rho_0 \left[1 - \alpha(T - T_0) \right] \tag{4}$$

where α denotes the coefficient of thermal expansion and ρ_0, the reference density (at $T = T_0$), varies depending on the material composition. The values used for the modelling parameters that remain constant are listed in Table 1.

The system of equations is solved using the arbitrary Lagrangian–Eulerian (ALE) finite element method (Hirt *et al.* 1974; Fullsack 1995). The model is set up by defining disparate material (chemical) domains and properties on a high resolution Lagrangian mesh which initially comprises a series of regular rectangular four-node elements. This information is mapped to an associated Eulerian mesh where the governing equations (above) are solved for updated fields of flow velocity $\mathbf{v}$ and temperature T for the given material configuration. These updated variables, in turn, are mapped back to the Lagrangian grid and the interpolated velocity at each node

Table 1. Common parameters used in all experiments.

Parameter		Value
ρ_0 (crust)	Crust reference density	2.8×10^3 kg m^{-3}
ρ_0 (mantle)	Mantle reference density	3.3×10^3 kg m^{-3}
c_p	Specific heat	1.25×10^3 J kg^{-1} K^{-1}
k	Thermal conductivity	5 W m^{-1} K^{-1}
g	Gravity acceleration	10 m s^{-2}
T_0	Reference temperature	293 K
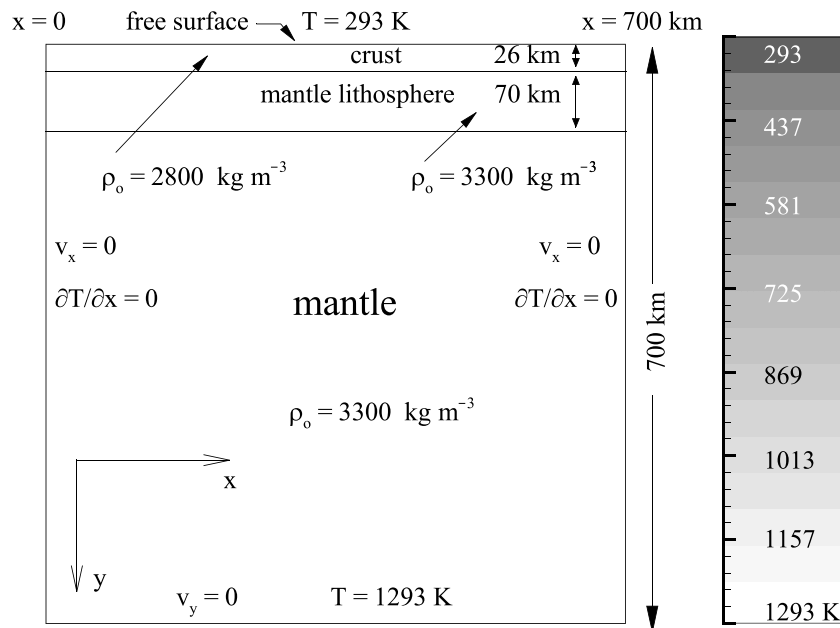
Figure 1. Set-up of the numerical experiments. Initial geotherm is plotted at right showing the contour scale used for temperature in all figures. See text for definition of the modelling parameters.

point is used to advect the Lagrangian mesh. The coupled Eulerian–Lagrangian interaction is repeated at every time step. The Eulerian mesh remains essentially undeformed (except for minor vertical dilation associated with the evolving free surface; see Appendix A) and therefore is used as the 'solver grid', whereas the advecting Lagrangian mesh acts as a 'tracker grid' that continues to follow the deforming material domains. This technique is useful for treating high strain materials (e.g. the convecting mantle) and for explicitly tracking moving material interfaces, such as the free surface and internal chemical boundaries. (See Fullsack 1995, for details of the implementation of the method and application to general tectonic problems.) The numerical routine has been benchmarked rigorously with previous convection studies to verify its accuracy and we present a comparison of values of free surface topography derived from the model with published benchmarks in Appendix A.

Fig. 1 shows the set-up of the idealized model for the upper mantle and crust. The solution space is 700 km deep with a buoyant viscous crust of thickness 26 km overlying the mantle; a strong mantle lithosphere (i.e. subcrustal lithosphere) of thickness 70 km is included in several of the numerical experiments, as described below. The density of the computational elements has been concentrated in the topmost 120 km of the models to increase the stability and accuracy of the lithospheric deformation and surface topography. The top boundary of the box is a free surface (see Appendix A) and all the other sides are free slip. The temperatures at the top surface and bottom boundary are kept constant at 293 K and 1293 K, respectively and the initial geotherm for all models is plotted in Fig. 1. Rather than attempting an exact simulation of the thermal state in the Earth's interior, this temperature range was chosen to correspond with the benchmark models for comparison (Appendix A).

Counter-clockwise mantle overturn of the density instability is initiated by imposing a small sinusoidal perturbation in the temperature field. In this way, the models are generally conditioned to have a downwelling plume at $x = 0$ and an upwelling plume at $x = 700$ km, although the pattern of flow varies in the time-dependent

systems. We conduct a series of experiments having various prescribed viscous rheologies for the crust (η_c) and mantle lithosphere (η_{ml}) and focus in particular on the evolution of the crust and surface topography above the downwelling plume at $x = 0$.

3 MODELLING RESULTS

3.1 Experiment set A: a buoyant crust

In the first set of experiments, a Newtonian temperature-independent rheology is used for the crust and the mantle. The mantle, including the mantle lithosphere, has a constant viscosity of $\eta_{ml} = \eta_m = 2.5 \times 10^{20}$ Pa s. As rough end-members, we consider two models: one with a strong crust, $\eta_c = 2.5 \times 10^{25}$ Pa s, and the other with a weak crust, $\eta_c = 2.5 \times 10^{22}$ Pa s. In both models, the mantle flow is dominated by a single convection cell with a descending cold plume at $x = 0$ and an ascending hot plume at $x = 700$ km (Figs 2a and 3a). Smaller wavelength boundary layer instabilities develop during this continued counter-clockwise mantle overturn.

For the strong crust model, A1, the surface topography consistently shows negative surface deflection above the downwelling plume at $x = 0$ and positive deflection above the rising plume at $x = 700$ km (Fig. 2b). The development of shorter-wavelength transient topographic undulations is due to smaller boundary layer instabilities evolving in the model.
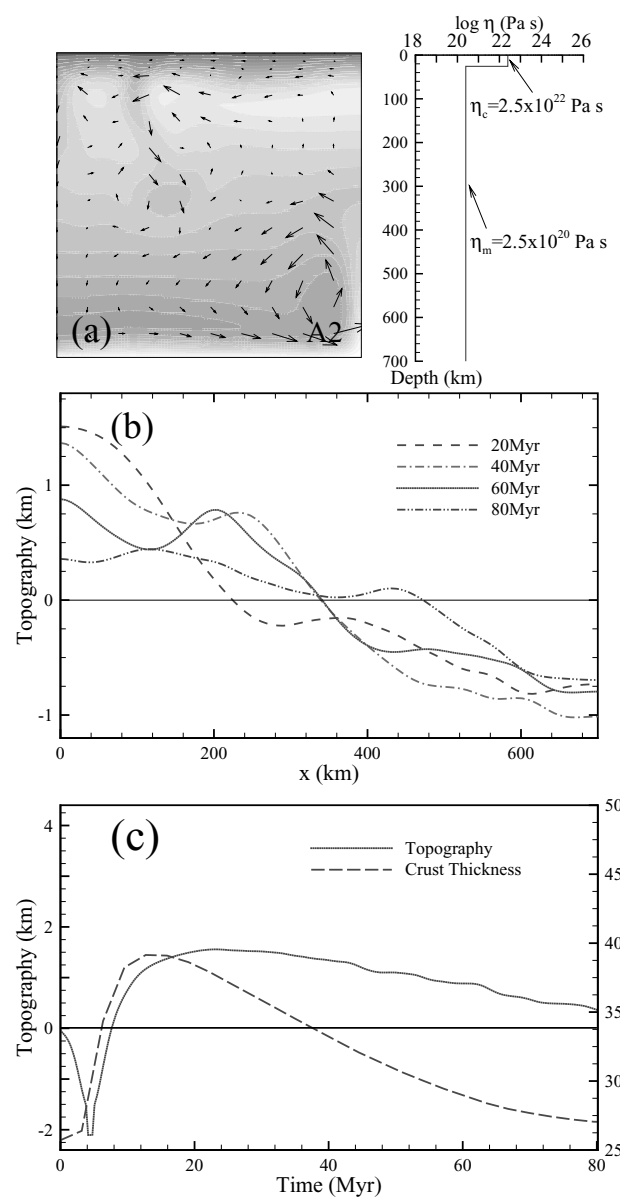
Fig. 2(c) plots the elevation of the surface and the thickness of the crust at $x = 0$ as a function of time. The topography reaches approximately -2400 m by $\sim t = 5$ Myr as the crust responds to the vigorous initial convective overturn in the model. The surface rises to -250 m at $t = 20$ Myr and remains relatively constant through the rest of the experiment. The thickness of the crust does not change as the model progresses; aside from the vertical motions driven by the underlying mantle flow, the crust remains undeformed. This behaviour of the strong crust model, namely constant negative topography induced by a descending plume, is generally consistent with predictions from mantle-flow models that neglect
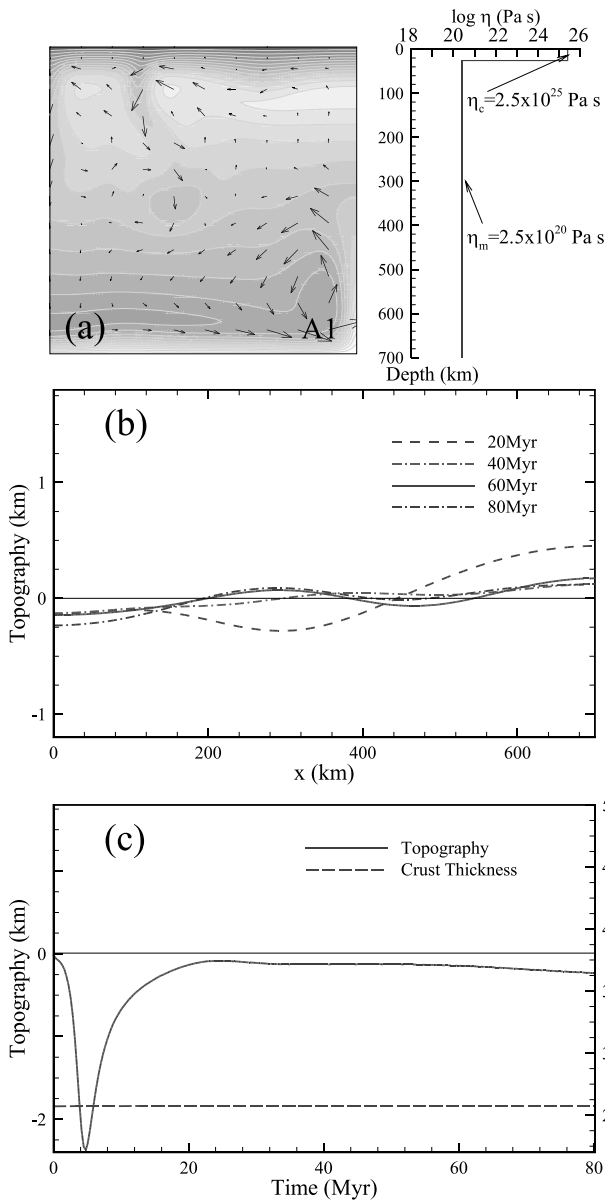
Figure 2. Model results for strong crust experiment A1: (a) temperature field and flow velocity vectors at 40 Myr, initial viscosity distribution at right; (b) profiles of surface topography at discrete time intervals (c) evolution of the surface topography and crustal thickness at $x = 0$.

Figure 3. Model results for weak crust experiment A2: (a) temperature field and flow velocity vectors at 40 Myr, initial viscosity distribution at right; (b) profiles of surface topography at discrete time intervals; (c) evolution of the surface topography and crustal thickness at $x = 0$.

a deformable crust (e.g. McKenzie *et al.* 1974; Blankenbach *et al.* 1989). However, the peak to peak amplitude of topography, ∼500 m, is considerably lower than in isoviscous models of similar convective vigour (see Appendix A) because of the presence of the strong crust in A1.

In experiment A2, where the viscosity of the crust has been lowered to $\eta_c = 2.5 \times 10^{22}$ Pa s, the surface expression of the mantle dynamics is significantly different. As shown in Fig. 3(b), the topography above the downwelling plume (at $x = 0$) is positive and the topography above the upwelling at $x = 700$ km is negative at each of the four time steps. During the initial convective overturn, the surface elevation at $x = 0$ subsides markedly; this subsidence recovers to a maximum uplift of ∼1600 m before slowly decreasing with time after $t = 25$ Myr (Fig. 3c). The time-series of crustal thickness at $x = 0$ provides insight into this behaviour. From

the initial value of 26 km, the crust rapidly thickens to 39 km in ∼15 Myr. The deformable crust responds to the horizontal stresses of the underlying counter-clockwise mantle circulation, which causes contraction and thickening of the buoyant crust at the left side of the convection cell above the downwelling plume. The crustal thickening and associated isostatic uplift at $x = 0$ eventually overcomes the subsidence induced by the mantle downwelling leading to an uplift of the surface.

The uplifted 'orogen' subsequently subsides and the crust gradually thins during the final 65 Myr of the experiment. These events are related to a decrease in the vigour of convection for the system. As the horizontal stresses that cause convergence and crustal thickening at $x = 0$ are reduced, the crust undergoes slow gravitational collapse by distributed viscous relaxation.

The results are consistent with the style of predicted surface topography in previous isoviscous ($\eta_c = \eta_{ml} = \eta_m$) models of

crust–mantle convection (Moresi & Lenardic 1997, 1999). However, owing to the weak crust in these models, the crust became more highly deformed (e.g. resulting in amplitudes of surface topography of −10 to +7.5 km) and experienced a more immediate response to the horizontal mantle convective forcings than in experiment A2.

3.2 Experiment set B: crust and mantle lithosphere

The preceding set of experiments and previous models (e.g. Moresi & Lenardic 1997) have considered the evolution of a buoyant crust above an isoviscous mantle. This approximation assumes that only the crust is 'plate-like', although lithospheric strength extends to depths of ~100–150 km within continental regions. We incorporate into the model a mantle lithosphere, approximating it as a 70 km thick layer beneath the crust. This region has the same properties as the underlying mantle, except it is assigned a different (constant) viscosity, η_{ml}. A sequence of models with various combinations of η_c and η_{ml} are examined.

In experiment B1 both the crust and mantle lithosphere have a viscosity of 2.5×10^{25} Pa s. As shown in Fig. 4(a), convective motion is now limited to depths greater than 100 km, i.e. below the strong lithosphere. Profiles of surface topography show a broad subsidence over the downwelling portion of the convection cell and a broad uplift over the upwelling (Fig. 4b). At $x = 0$ the surface elevation falls rapidly to −1000 m (owing to the initial convective overturn), but recovers, rapidly at first to −400 m and then more gradually to −100 m over the course of the model run. The thickness of the crust remains constant at 26 km (Fig. 4c). Since the strong lithosphere is unable to deform, the surface topography is governed by deflection associated with the vertical component of the mantle convective stresses alone. Note that short lengthscale topographical variations, as observed in the first set of experiments (series A), are absent in B1. In this case, the strong lithosphere is of sufficient thickness to filter out these short-wavelength features.

We next consider a weaker lithosphere (experiment B2) by setting $\eta_c = \eta_{ml} = 2.5 \times 10^{22}$ Pa s. As in B1, convective fluid motion is primarily restricted to the sub-lithospheric mantle, and is dominated by a counter-clockwise circulation cell (Fig. 5a). A long-wavelength surface topography develops in response to this convective forcing. The orientation of topography is opposite to the results in experiment B1; a positive elevation develops above the downwelling at the left side of the convection space and a negative elevation forms above the return upwelling at the right side (Fig. 5b). After an initial subsidence, the surface topography at $x = 0$ quickly recovers to a positive elevation and then increases gradually to reach ~1500 m by 80 Myr (Fig. 5c). The undulations in the topography (with period ~10 Myr) are due to the quasi-periodic development of smaller-scale thermal instabilities in the mantle. Once again, the time-dependent evolution of topography above the mantle downwelling is governed by the response of the crust and mantle lithosphere to both vertical and horizontal mantle forcings. The downwelling mantle plume induces dynamic subsidence of the crust (e.g. first 10 Myr; Fig. 5c), but the mantle circulation simultaneously entrains the lithosphere in a horizontal direction towards $x = 0$. This compression causes significant thickening of the deformable lithosphere above the descending plume. By $t \simeq 13$ Myr, this thickening and resultant uplift overcomes the dynamic subsidence supported by the mantle flow and the topography at $x = 0$ becomes positive.

As crustal thickening continues, the surface topography at this point continues to rise, although the rate of uplift decreases as grav-
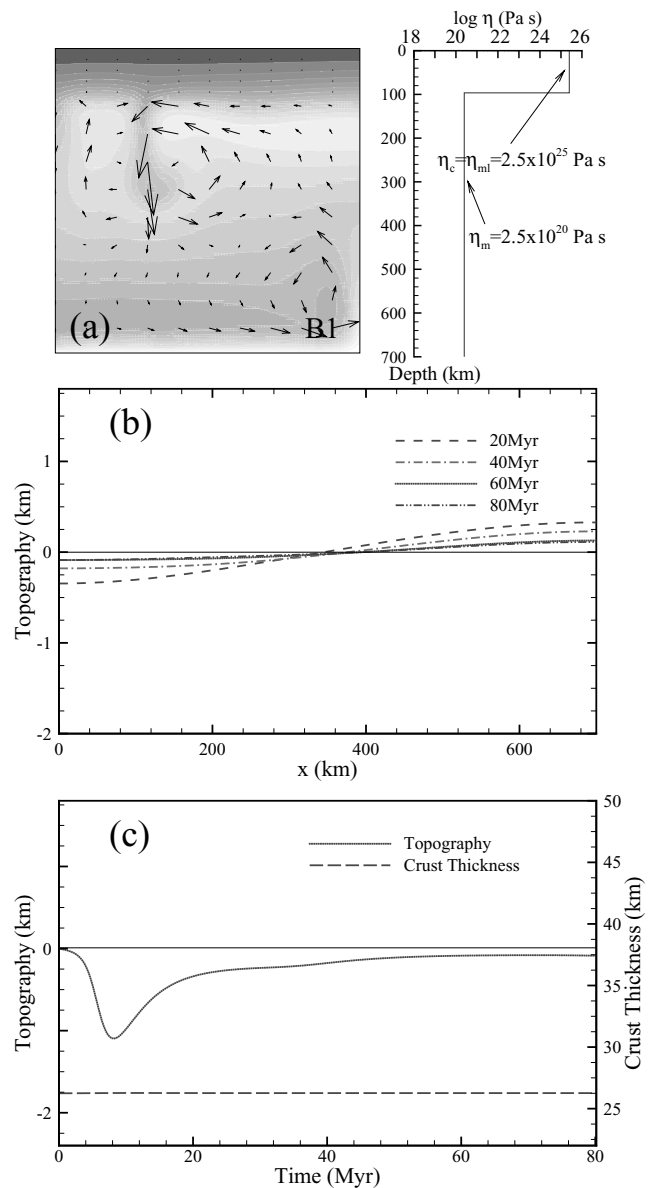
Figure 4. Model results for strong crust/strong mantle lithosphere experiment B1: (a) temperature field and flow velocity vectors at 40 Myr, initial viscosity distribution at right; (b) profiles of surface topography at discrete time intervals (c) evolution of the surface topography and crustal thickness at $x = 0$.

itational forces limit the height of the viscous model orogen. The crust has not reached the subsidence/thinning phase at $x = 0$ as demonstrated in experiment A2. The presence of a thick, relatively strong mantle lithosphere delays response of the crust to the sub-lithospheric mantle forcing (e.g. also compare timescale for crustal thickening between A2 and B2).

Experiment B3 considers a combination of lithospheric viscosities with $\eta_c = 2.5 \times 10^{22}$ Pa s and $\eta_{ml} = 2.5 \times 10^{25}$ Pa s. The evolution of the model is very similar to experiment B1. Namely, surface topography is characterized by long-wavelength negative deflection above the downwelling mantle flow and uplift above the upwelling (Fig. 6b). Although the crust is relatively weak, it remains at a constant thickness of 26 km (Fig. 6c). Not surprisingly, the behaviour of the lithosphere is controlled by its high-strength component, the mantle lithosphere. Essentially this strong layer insulates the weak
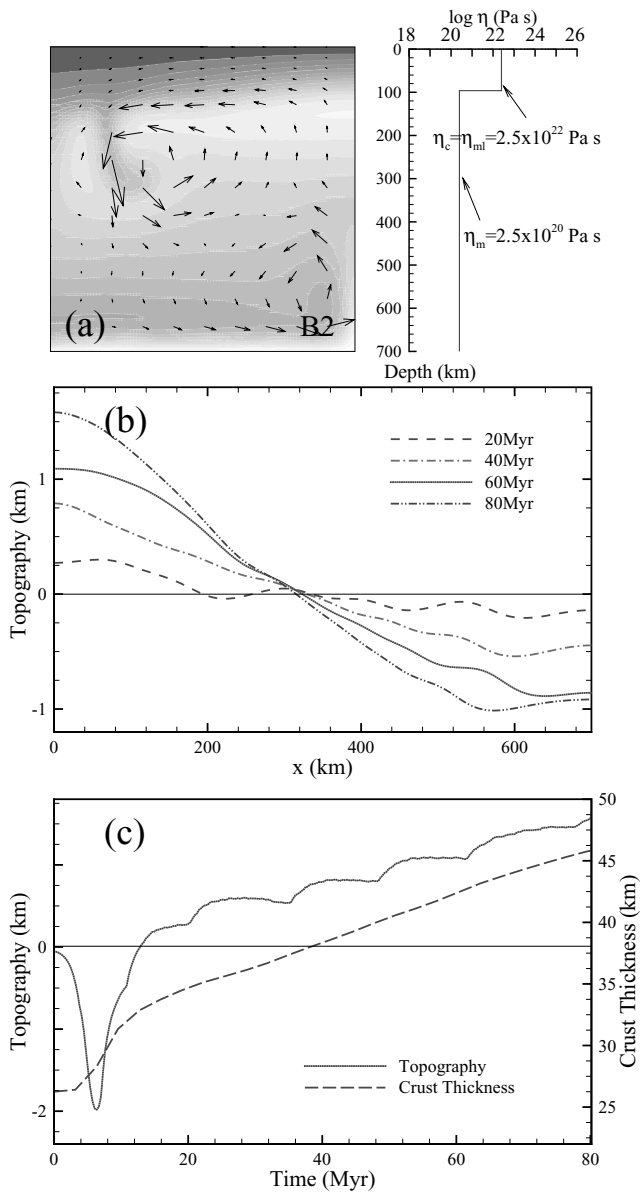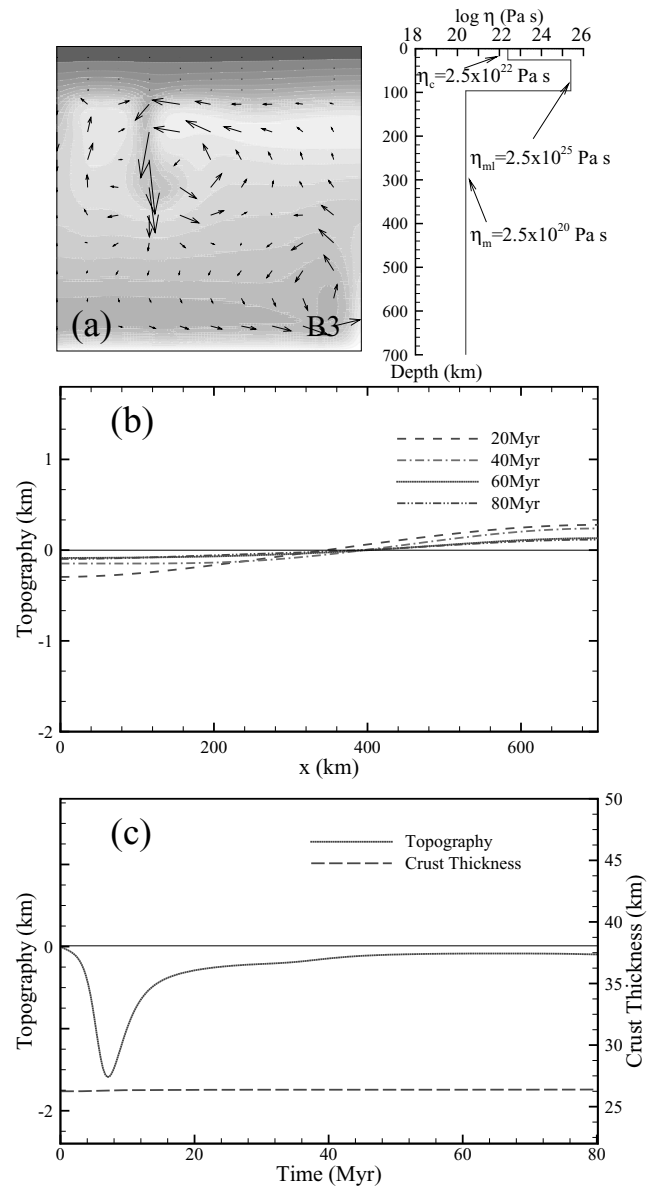
Figure 5. Model results for weak crust/weak mantle lithosphere experiment B2: (a) temperature field and flow velocity vectors at 40 Myr, initial viscosity distribution at right; (b) profiles of surface topography at discrete time intervals (c) evolution of the surface topography and crustal thickness at $x = 0$.

Figure 6. Model results for weak crust/strong mantle lithosphere experiment B3: (a) temperature field and flow velocity vectors at 40 Myr, initial viscosity distribution at right; (b) profiles of surface topography at discrete time intervals (c) evolution of the surface topography and crustal thickness at $x = 0$.

crust from convection-driven horizontal deformation, although the lithosphere as a whole undergoes vertical motions under the effect of the underlying mantle flow. This suggests that the rheology of the strongest layer in the lithosphere will be the controlling factor in the process.

3.3 Experiment set C: temperature-dependent rheologies

The preceding models considered the dynamics of a crust–mantle system comprised of separate isoviscous regions. However, it is clear from experimental studies that the crust and mantle materials have a strongly temperature-dependent rheology (e.g. Ranalli 1987). In the following set of numerical experiments, we modify our crust, mantle lithosphere and mantle regions to incorporate a temperature-

dependent viscosity of the form:

$$\eta = \eta_0 \exp(-T/b) \tag{5}$$

The parameters b and η_0 used in the experiments and the relevant viscosity ranges are given in Table 2. For all the models, the rheological definition of the mantle (including mantle lithosphere) is identical, although obviously the viscosity profile varies depending on the style of thermal convection.

For experiment C1, we prescribe a strong crust, which reaches a maximum viscosity of 10^{25} Pa s at the surface. The mantle flow is again dominated by a counter-clockwise convection cell, although localized convective flow results in a narrow downwelling along the right side of the solution space. The topography profiles show a subsidence of ∼1 km above the mantle downwelling and uplift above the upwelling (Fig. 7b). Subsidence at $x = 0$ is maintained

Table 2. Parameters for temperature-dependent Newtonian rheology used in the third set of experiments (SI).

Region	b	η_0 (Pa s)	Viscosity range (Pa s)
Mantle (C1 and C2)	91.53	1.37×10^{24}	10^{18}–10^{22}
High viscosity crust (C1)	13.64	2.13×10^{34}	10^{20}–10^{25}
Low viscosity crust (C2)	34.09	5.40×10^{25}	10^{20}–10^{22}
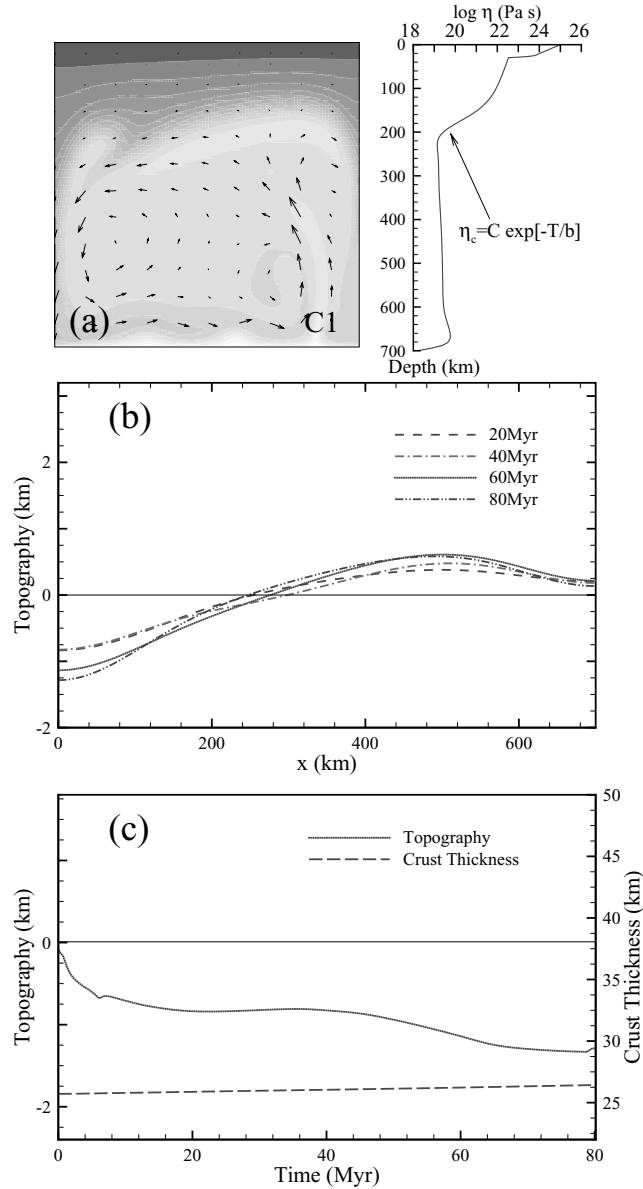
Figure 7. Model results for strong crust temperature-dependent rheology experiment C1: (a) temperature field and flow velocity vectors at 40 Myr, horizontally averaged viscosity distribution at right; (b) profiles of surface topography at discrete time intervals (c) evolution of the surface topography and crustal thickness at $x = 0$.

above the descending plume since, as in previous models having a strong crust, the thickness of the crust does not significantly vary during the evolution of the model (Fig. 7c).

The viscosity parameters chosen for experiment C2 result in a weaker crust and mantle lithosphere. The horizontally averaged viscosity of the crust peaks at 10^{22} Pa s at the surface and is an order
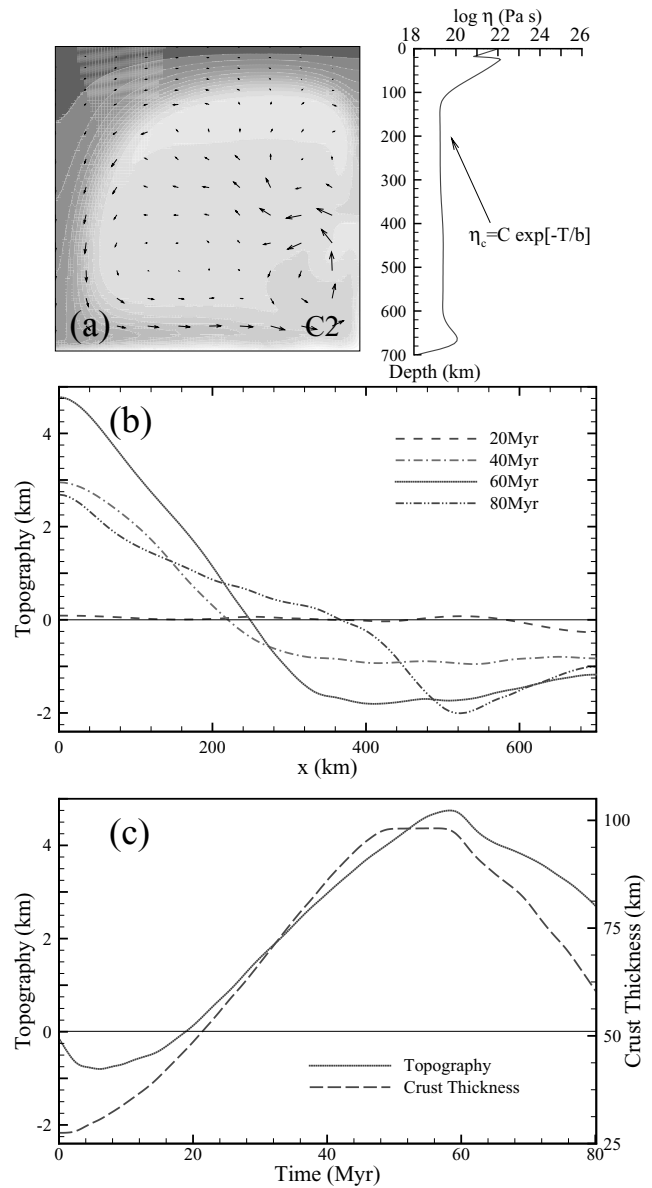
Figure 8. Model results for moderate strength crust temperature-dependent rheology experiment C2: (a) temperature field and flow velocity vectors at 40 Myr, horizontally averaged viscosity distribution at right; (b) profiles of surface topography at discrete time intervals (c) evolution of the surface topography and crustal thickness at $x = 0$.

of magnitude lower than this in the warmer lower crust at a depth of 30 km (Fig. 8a). The underlying mantle lithosphere has a maximum average viscosity of 2×10^{22} Pa s and decreases with depth into the higher temperature mantle. Convective flow is primarily limited to the mantle (i.e. depths >100 km), but portions of the weak lower lithosphere are also entrained in the circulating cell (e.g. $x \simeq$ 500 km; Fig. 8a). Although topographic undulations at $t = 20$ Myr are modest, by $t = 60$ Myr a significant uplift develops over the mantle downwelling while the remainder of the surface is depressed (Fig. 8b). Again, this is due to the mantle flow-induced thickening of the buoyant crust at $x = 0$, which reaches a maximum thickness of 97 km above the downwelling (Fig. 8c).

The high topography in experiment C2 is not sustained, but instead rapidly decreases for $t > 60$ Myr (Fig. 8c). Over this stage, the
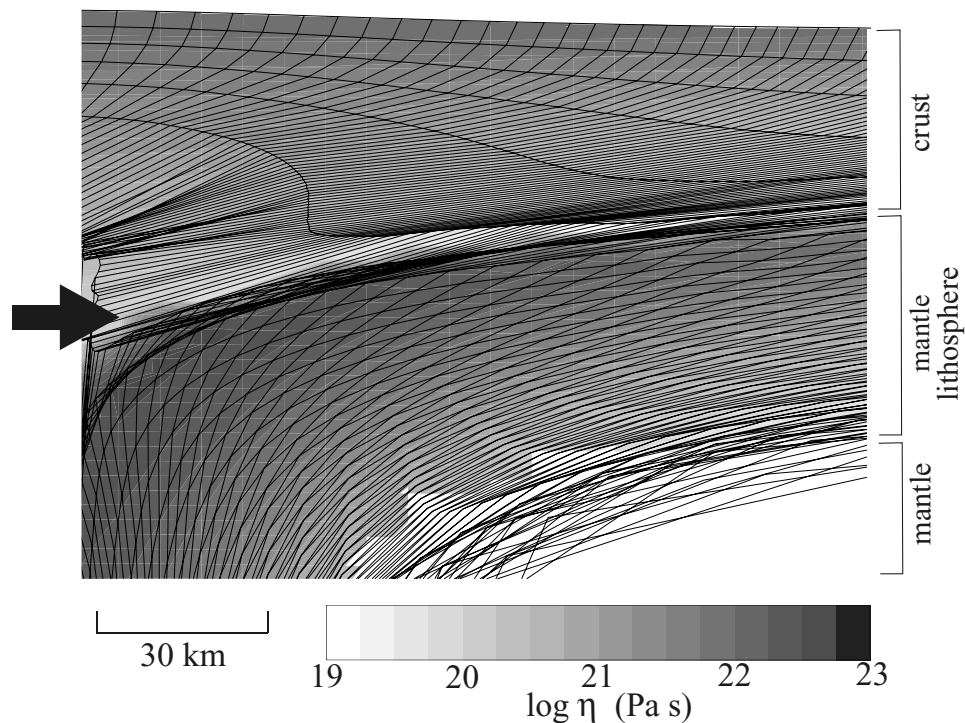
Figure 9. Shaded contour plot of log of viscosity for experiment C2. Zoom to top left portion of solution space above the mantle downwelling. Arrow indicates position of low viscosity region in lower crust. Lagrangian grid is superimposed to show deformation of material; note high deformation in lower crust (extremely stretched elements have not been plotted).

model orogen subsides as gravitational forces overcome the strength of the uplifted crust and the crust consequently thins above the downwelling. While the topographic collapse is similar to that shown in model A2, it occurs by a very different process because of the temperature-dependent rheology in C2. Fig. 9 plots the deformed Lagrangian mesh and viscosity of the model at $t = 80$ Myr, zooming in on the top left portion of the solution space. It is clear that a low-viscosity region has developed in the hot base of the thickened crust. Deformation of the crust has started to localize in this region (note the distortion of Lagrangian grid) indicating that collapse of the high surface elevation is achieved by flow in the low-viscosity lower crust. This behaviour is akin to the style of syn-convergent topographic 'deflation' by ductile flow in the lower crust that has been postulated for certain orogenic settings (Beaumont *et al.* 2001; Vanderhaeghe & Teyssier 2001).

4 CONCLUSIONS/DISCUSSION

Our series of experiments provide further insight into the importance of crust–mantle interactions in the evolution of mantle flow-driven surface topography. Namely, over geological timescales the surface topography is governed by the tandem effects of dynamic topography supported by convection in the sublithospheric mantle and deformation of the crust associated with convection-induced horizontal stresses. However, the response of the crust is highly dependent on its rheology and the strength of the mantle lithosphere.

A strong crust is able to resist internal deformation and the surface topographical response is, in this case, dominated by vertical motions induced by the mantle flow (e.g. process (1); Fig. 10). These experiments are consistent with mantle convection models which neglect the coupled behaviour of a buoyant crust and predict, for
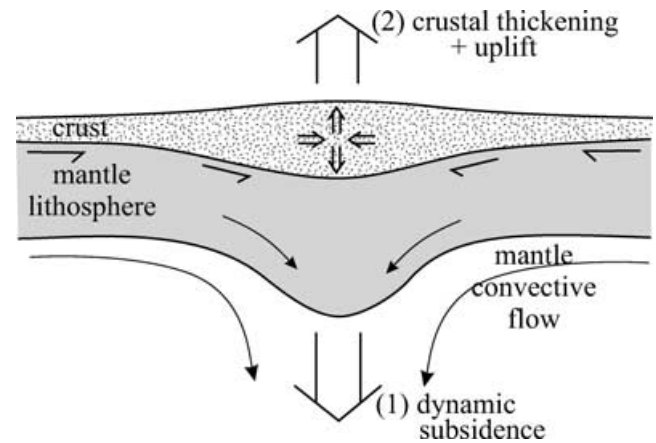
Figure 10. Schematic illustrating the processes contributing to surface topography during an episode of mantle downwelling.

example, continued subsidence above a downwelling plume for as long as the plume persists. A weaker crust is able to deform in response to horizontal stresses induced by the underlying mantle flow (e.g. Moresi & Lenardic 1997; Zhong 1997). As illustrated schematically in Fig. 10, the surface topography above a mantle downwelling is governed by the combined effect of (1) dynamic subsidence supported by underlying mantle flow, and (2) uplift due to flow-induced crustal thickening. The interaction of these processes results in a strong time-dependence of surface topography. For example, our numerical experiments indicate that the onset of descending mantle flow below a deformable crust leads, initially, to subsidence by process (1) followed by uplift as process (2) begins to dominate. The presence of a strong mantle lithosphere beneath

a weak crust, however, is able to 'insulate' the crust from the underlying horizontal mantle flow. In this case, the crust and mantle lithosphere respond primarily to the normal convective stresses at the base of the lithosphere and undergo dynamic subsidence above a mantle downwelling.

The time-dependent evolution of crustal deformation is also strongly influenced by a temperature-dependent rheology for the crust. Subsequent to thickening and uplift of a deformable crust, the model orogen may rapidly deflate as subsidence and crustal thinning become dominant (Fig. 8c). This is accommodated by localized ductile flow in the hot low-viscosity lower crust in a direction away from the centre of crustal thickening/uplift. Alternatively, partial topographic collapse may occur by distributed viscous flow of the crust as a whole if the horizontal mantle convective forcing that supports the thickened crust is diminished (Fig. 3c). Thus the models predict that these styles of topography/crustal deformation are transient features which rely on continued underlying convective stresses. However, we have not included elastic/plastic rheologies in the model lithosphere which may provide improved 'mechanical support' for sustaining topography. Furthermore, we ignore the influence of chemical alterations and the associated buoyancy effect which may increase the stability of the thickened lithospheric root (Lenardic & Moresi 1999).

Our models focus on an upper mantle scale (i.e. <700 km depth) of thermal convection as the driving force for crustal motion/deformation. Such 'small-scale convection' may be an active process in various tectonic regimes (e.g. Boutilier & Keen 1999; Solomatov & Moresi 2000). In particular, King & Ritsema (2000) suggest that small-scale convection can develop beneath cratonic regions as a style of edge-driven convection associated with changes in lithospheric thickness. Thus, it may not be necessary to invoke major tectonic processes, such as plate subduction or continental rifting, to account for localized mantle flow. Furthermore, small-scale convection may be the precursor to subsequent gravitational instability of the lithosphere which may enhance the resultant crustal dynamics (Marotta *et al.* 1999; Neil & Houseman 1999). A series of experiments were also conducted in which we assumed deeper depths (1000 and 2000 km) of mantle convection in a larger numerical boxes. In these models, the magnitude and style of topography variations and crustal deformation above downwelling mantle flows was consistent with the results with the 700 km deep mantle. With models with a deeper mantle, however, the topography above the upwelling at the right side of the solution space in each of the models was more subdued than in the upper mantle models. The crustal deformation/topography was driven primarily by the downwelling flow, and in a larger convection space the associated return-flow upwelling has a decreased influence on crustal dynamics. These differences in the return-flow have negligible effects on the crustal evolution and topography above the downwelling at $x = 0$.

The modelling results have particular implications for relatively weak crustal environments (i.e. $\eta_c = 10^{22}$–10^{23} Pa s), but generally the crust and the lithosphere as a whole are strong (Kohlstedt *et al.* 1995) especially in plate interiors (Zoback & Townend 2001). Weakening of continental lithosphere is usually associated with large-scale regions of high flow, such as rift environments. However, the strength of the crust can also be significantly reduced due to local thermal/tectonic effects. McLaren *et al.* (1999), for example, suggest that the Proterozoic burial of highly radioactive granites in the Mount Isa region of Australia may have resulted in an increase in the crustal geotherm thereby inducing regional weakening of the lithosphere. Similar processes of high heat flow and

effective crustal weakening has also been inferred for other cratons (Russell & Kopylova 1999). Inherent mechanical weak zones associated with the tectonic assemblage of a particular region may also be an important control on the local strength of the lithosphere (Lankreijer *et al.* 1997).

For the numerical experiments, we have defined a simplified, rheologically homogeneous crust in order to facilitate interpretation of the results. A more 'realistic' crust may include, for example, lateral heterogeneities, radiogenic heating, and more complex rheologies (e.g. non-Newtonian viscous, incorporating an elastic/plastic response); a further suite of experiments based on such refinements to the model crust is currently under study. Nevertheless, the idealized models presented here serve to illustrate the fundamental dynamics of the crust–mantle interactions.

REFERENCES

Beaumont, C., Jamieson, R.A., Nguyen, M.H. & Lee, B., 2001. Himalayan tectonics explained by extrusion of a low-viscosity crustal channel coupled to focused surface denudation, *Nature,* **414,** 738–742.

Bercovici, D., 1998. Generation of plate tectonics from lithosphere-mantle flow and void-volatile self-lubrication, *Earth planet. Sci. Lett.,* **154,** 139–151.

Bercovici, D., Ricard, Y. & Schubert, G., 2001. A two-phase model for compaction and damage, 3. Applications to shear localization and plate boundary formation, *J. geophys. Res.,* **106,** 8925–8940.

Blankenbach, B. *et al.*, 1989. A benchmark comparison for mantle convection codes, *Geophys. J. Int.,* **98,** 23–38.

Boutilier, R.R. & Keen, C.E., 1999. Small-scale convection and divergent plate boundaries, *J. geophys. Res.,* **104,** 7389–7403.

Fleitout, L. & Froidevaux, C., 1982. Tectonics and topography for a lithosphere containing density heterogeneities, *Tectonics,* **1,** 21–56.

Forte, A.M., Peltier, W.R., Dziewonski, A.M. & Woodward, R.L., 1993. Dynamic surface topography; a new interpretation based upon mantle flow models derived from seismic tomography, *Geophys. Res. Lett.,* **20,** 225–228.

Fullsack, P., 1995. An arbitrary Lagrangian-Eulerian formulation for creeping flows and its application in tectonic models, *Geophys. J. Int.,* **120,** 1–23.

Gurnis, M., 1992. Rapid continental subsidence following the initiation and evolution of subduction, *Science,* **255,** 1556–1558.

Gurnis, M., Eloy, C. & Zhong, S., 1996. Free-surface formulation of mantle convection-II. Implications for subduction-zone observables, *Geophys. J. Int.,* **127,** 719–727.

Gurnis, M., Mitrovica, J.X., Ritsema, J. & van Heijst, H.-J., 2000. Constraining mantle structure using geological evidence of surface uplift rates: The case of the African Superplume, *Geochem. Geophys. Geosys.,* **1**.

Hager, B.H., 1984. Subducted slabs and the Geoid: Constraints on mantle rheology and flow, *J. geophys. Res.,* **89,** 6003–6015.

Hager, B.H. & O'Connell, R.J., 1981. A simple global model of plate dynamics and mantle convection, *J. geophys. Res.,* **86,** 4843–4867.

Hager, B.H., Clayton, R.W., Richards, M.A., Comer, R.P. & Dziewonski, A.M., 1985. Lower mantle heterogeneity, dynamic topography and the geoid, *Nature,* **313,** 541–545.

Hirt, C.W., Amsden, A.A. & Cook, J.L., 1974. An arbitrary Lagrangian-Eulerian computing method for all flow speeds, *J. Comput. Phys.,* **14,** 227–253.

King, S.D. & Ritsema, J., 2000. African hot spot volcanism: Small-scale convection in the upper mantle beneath cratons, *Science,* **290,** 1137–1140.

Kohlstedt, D.L., Evans, B. & Mackwell, S.J., 1995. Strength of the lithosphere: Constraints imposed by laboratory experiments, *J. geophys. Res.,* **100,** 17 587–17 602.

Lankreijer, A., Mocanu, V. & Cleotingh, S., 1997. Lateral variations in lithosphere strength in the Romanian Carpathians: constraints on basin evolution, *Tectonophys.,* **272,** 269–290.

Lenardic, A. & Kaula, W.M., 1995. More thoughts on convergent crustal plateau formation and mantle dynamics with regard to Tibet, *J. geophys. Res.,* **100,** 15 193–15 203.

Lenardic, A. & Kaula, W.M., 1996. Near-surface thermal/chemical boundary layer convection at infinite Prandtl number: two-dimensional numerical experiments, *Geophys. J. Int.,* **126,** 689–711.

Lenardic, A. & Moresi, L.-N., 1999. Some thoughts on the stability of cratonic lithosphere: Effects of buoyancy and viscosity, *J. geophys. Res.,* **104,** 12 747–12 758.

Lenardic, A., Kaula, W.M. & Bindschadler, D.L., 1993. A mechanism for crustal recycling on Venus, *J. geophys. Res.,* **98,** 18 697–18 705.

Lenardic, A., Kaula, W.M. & Bindschadler, D.L., 1995. Some effects of a dry crustal flow law on numerical simulations of coupled crustal deformation and mantle convection on Venus, *J. geophys. Res.,* **100,** 16 949–16 957.

Lithgow-Bertelloni, C. & Silver, P.G., 1998. Dynamic topography, plate driving forces and the African superswell, *Nature,* **395,** 269–272.

Marotta, A.M., Fernandez, M. & Sabadini, R., 1999. The onset of extension during lithospheric shortening: a two-dimensional thermomechanical model for lithospheric unrooting, *Geophys. J. Int.,* **139,** 98–114.

McLaren, S., Sandiford, M. & Hand, M., 1999. High radiogenic heat-producing granites and metamorphism—An example from the western mount Isa inlier, Australia, *Geology,* **27,** 679–682.

McKenzie, D.P., 1977. Surface deformation, gravity anomalies and convection, *Geophys. J. R. astr. Soc.,* **48,** 211–238.

McKenzie, D.P., Roberts, J.M. & Weiss, N.O., 1974. Convection in the Earth's mantle: towards a numerical solution, *J. Fluid Mech.,* **62,** 465–538.

Mitrovica, J.X., Beaumont, C. & Jarvis, G.T., 1989. Tilting of continental interiors by the dynamical effects of subduction, *Tectonics,* **8,** 1079–1094.

Moresi, L. & Lenardic, A., 1997. Three-dimensional numerical simulations of crustal deformation and subcontinental mantle convection, *Earth planet. Sci. Lett.,* **150,** 233–243.

Moresi, L. & Lenardic, A., 1999. Three-dimensional mantle convection with contiental crust: First-generation numerical simulations, *Earth Int.,* **3,** 1–14.

Moresi, L. & Solomatov, V., 1998. Mantle convection with a brittle lithosphere: thoughts on the global tectonic styles of the Earth and Venus, *Geophys. J. Int.,* **133,** 669–682.

Neil, E.A. & Houseman, G.A., 1999. Rayleigh–Taylor instability of the upper mantle and its role in intraplate orogeny, *Geophys. J. Int.,* **138,** 89–107.

Poliakov, A. & Podladchikov, Y., 1992. Diapirism and topography, *Geophys. J. Int.,* **109,** 553–564.

Pysklywec, R.N. & Mitrovica, J.X., 1998. A mantle flow mechanism in the long-wavelength subsidence of continental interiors, *Geology,* **26,** 687–690.

Pysklywec, R.N. & Mitrovica, J.X., 1999. The role of subduction-induced subsidence in the evolution of the Karoo Basin, *J. Geol.,* **107,** 155–164.

Pysklywec, R.N. & Quintas, M.C.L., 2000. A mantle flow mechanism for the late Paleozoic subsidence of the Parana Basin, *J. geophys. Res.,* **105,** 16 359–16 370.

Ranalli, G., 1987. *Rheology of the Earth,* Allen & Unwin Press, Boston.

Russell, M. & Gurnis, M., 1994. The planform of epeirogeny: Vertical motions of Australia during the Cretaceous, *Basin Res.,* **6,** 63–76.

Russell, J.K. & Kopylova, M.G., 1999. A steady state conductive geotherm for the north central Slave, Canada: Inversion of petrological data from the Jericho Kimberlite pipe, *J. geophys. Res.,* **104,** 7089–7101.

Smrekar, S.E. & Parmentier, E.M., 1996. The interaction of mantle plumes with surface thermal and chemical boundary layers: Applications to hotspots on Venus, *J. geophys. Res.,* **101,** 5397–5410.

Solomatov, V.S. & Moresi, L.N., 2000. Scaling of time-dependent stagnant lid convection: Application to small-scale convection on Earth and other planets, *J. geophys. Res.,* **105,** 21 795–21 817.

Stern, T.A. & Holt, W.E., 1994. Platform subsidence behind an active subduction zone, *Nature,* **368,** 233–236.

Tackley, P.J., 1998. Self-consistent generation of tectonic plates in three-dimensional mantle convection, *Earth planet. Sci. Lett.,* **157,** 9–22.

Tackley, P.J., 2000a. Self-consistent generation of tectonic plates in time-dependent, three-dimensional mantle convection simulations, part 1: Pseudoplastic yielding, *Geochem. Geophys. Geosys.,* **1.**

Tackley, P.J., 2000b. Self-consistent generation of tectonic plates in time-dependent, three-dimensional mantle convection simulations, part 2: Strain weakening and asthenosphere, *Geochem. Geophys. Geosys.,* **1.**

Thoraval, C., Machetel, P. & Cazenave, A., 1995. Locally layered convection inferred from dynamic models of the Earth's mantle, *Nature,* **375,** 777–780.

Trompert, R. & Hansen, U., 1998. Mantle convection simulations with rheologies that generate plate-like behaviour, *Nature,* **395,** 686–689.

Vanderhaeghe, O. & Teyssier, C., 2001. Partial melting and flow of orogens, *Tectonophys.,* **342,** 451–472.

Zhong, S., 1997. Dynamics of crustal compensation and its influences on crustal isostasy, *J. geophys. Res.,* **102,** 15 287–15 299.

Zhong, S., Gurnis, M. & Moresi, L., 1996. Free-surface formulation of mantle convection-I. Basic theory and application to plumes, *Geophys. J. Int.,* **127,** 708–718.

Zoback, M.D. & Townend, J., 2001. Implications of hydrostatic pore pressures and high crustal strength for the deformation of intraplate lithosphere, *Tectonophys.,* **336,** 19–30.

APPENDIX A: FREE SURFACE TOPOGRAPHY AND BENCHMARKING

In most numerical mantle convection simulations, the evolution of surface topography is not derived directly in the mantle flow computation. Instead, it is approximated as the instantaneous deflection of a surface that would be supported by the normal viscous flow stresses calculated at the fixed top boundary of the solution space (e.g. McKenzie *et al.* 1974). This *a posteriori* calculation is required because these convective flow models impose a free-slip, zero vertical velocity boundary condition at the top surface:

$$v_y(y = 0) = 0; \quad \sigma_{xy}(y = 0) = 0 \tag{A1}$$

where σ_{xy} is the tangential stress (see Fig. 1 for component directions).

In the approach used here, we adopt an upper surface that is free to deform in response to the underlying dynamics (Fullsack 1995). At each time step, updated material velocities are derived from the (full weight) finite element solution for the viscous convecting system. There is no velocity constraint applied to the upper surface of the solution space and at the surface we allow for a free normal stress:

$$\boldsymbol{\sigma} \cdot \hat{n} = [\sigma_{yx}, \sigma_{yy}] = [0, 0] \tag{A2}$$

where $\hat{n}$ is the unit normal at the top surface. The vertical component of velocity that is computed along the 'free' top of the solution space is used to incrementally update the position of the top surface of the Eulerian grid (i.e. in the vertical direction) at each time step. The remainder of the Eulerian grid is then evenly remeshed by vertical dilation to accommodate this subtle motion of the top surface. In this way the evolving surface topography may
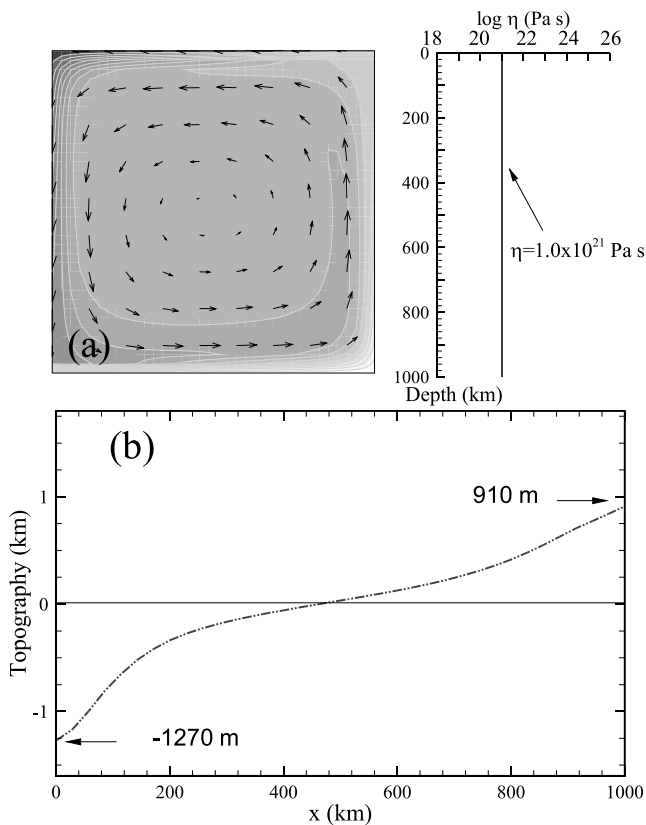
Figure A1. Model results for benchmark experiment: (a) temperature field and flow velocity vectors at 40 Myr, initial viscosity distribution at right; (b) profiles of surface topography at discrete time intervals (c) evolution of the surface topography and crustal thickness at $x = 0$.

be directly tracked during the mantle convection run. (For details of the numerical algorithms for mesh advection, interface tracking and regridding in the ALE finite element model see Fullsack 1995.)

The numerical code has been rigorously benchmarked against various 'fixed lid' convection experiments (Blankenbach *et al.* 1989) and for free-surface topography calculations (Poliakov & Podladchikov 1992). As a reference model for our numerical experiments, we set up a simple isoviscous convection run in a 10^3 km by 10^3 km square box, with no prescribed crust or mantle lithosphere, and having a Rayleigh number of 10^6. Thus, the experiment is identical to 'Case 1(c)' from Blankenbach *et al.* (1989), except that our model has a free top surface.

After it has reached steady state, the mantle flow is characterized by a counter-clockwise circulating cell (Fig. A1a). As expected, the surface topography along the top of the solution space shows a topography low over the downwelling at the left side of the box and a topography high over the upwelling at the right (Fig. A1b). The peak to peak topography amplitude of 2170 m is within 2 per cent of the 'best' value of 2215.76 m from Blankenbach *et al.* (1989). This amplitude is significantly higher than in model A1 which shows a qualitatively similar signal of topography since the presence of a strong crust in A1 effectively dampens the surface response to the underlying hydrodynamic stresses.

Other studies have shown that long-wavelength dynamic topography computed in free-surface calculations will be consistent with models with a fixed top surface and using *a posteriori* topography predictions (Poliakov & Podladchikov 1992). A method has also been devised for computing 'pseudo-free surface' topography above a convecting cell (Zhong *et al.* 1996; Gurnis *et al.* 1996). These models similarly suggest that a free-slip top surface boundary condition and *a posteriori* topography calculation is accurate except for cases of intermediate- and short-wavelength surface deflection or very high lithospheric strength.